Behavioral/Systems/Cognitive

Local Edge Detectors: A Substrate for Fine Spatial Vision at Low Temporal Frequencies in Rabbit Retina

Michiel van Wyk,[1] W. Rowland Taylor,[2] and David I. Vaney[1]

[1]Vision, Touch and Hearing Research Centre, School of Biomedical Sciences, Australian Research Council Centre of Excellence in Vision Science, University of Queensland, Brisbane, Queensland 4072, Australia, and [2]Neurological Sciences Institute, Oregon Health & Science University, Beaverton, Oregon 97006

Visual acuity is limited by the size and density of the smallest retinal ganglion cells, which correspond to the midget ganglion cells in primate retina and the β-ganglion cells in cat retina, both of which have concentric receptive fields that respond at either light-On or light-Off. In contrast, the smallest ganglion cells in the rabbit retina are the local edge detectors (LEDs), which respond to spot illumination at both light-On and light-Off. However, the LEDs do not predominate in the rabbit retina and the question arises, what role do they play in fine spatial vision? We studied the morphology and physiology of LEDs in the isolated rabbit retina and examined how their response properties are shaped by the excitatory and inhibitory inputs. Although the LEDs comprise only ~15% of the ganglion cells, neighboring LEDs are separated by 30–40 μm on the visual streak, which is sufficient to account for the grating acuity of the rabbit. The spatial and temporal receptive-field properties of LEDs are generated by distinct inhibitory mechanisms. The strong inhibitory surround acts presynaptically to suppress both the excitation and the inhibition elicited by center stimulation. The temporal properties, characterized by sluggish onset, sustained firing, and low bandwidth, are mediated by the temporal properties of the bipolar cells and by postsynaptic interactions between the excitatory and inhibitory inputs. We propose that the LEDs signal fine spatial detail during visual fixation, when high temporal frequencies are minimal.

Key words: **retinal ganglion cell; edge detection; rabbit retina; visual acuity; amacrine cell; inhibition**

Introduction

In the primate retina, the spatial resolving power is set by the midget ganglion cells, which account for 70–80% of the ganglion cells. In other mammalian retinas, homologous types of ganglion cells are thought to perform a similar function: in the well studied cat retina, the X-cells/β-cells account for ~50% of the ganglion cells (Wässle, 2004). However, it has yet to be demonstrated that fine spatial vision is mediated by such ganglion cells in other model species.

Although the rabbit retina contains brisk-sustained concentric cells that are similar to X-cells (Caldwell and Daw, 1978; Vaney et al., 1981), the ganglion cells with the smallest receptive fields are the local edge detectors (LEDs), which are encountered infrequently by extracellular recording electrodes (Levick, 1967). The small receptive field of LEDs is matched by a small dendritic field (Amthor et al., 1989), and correspondingly, several studies suggest that LEDs may be the commonest type of ganglion cell in the rabbit retina (DeVries and Baylor, 1997; Rockhill et al., 2002). However, there are at least a dozen types of ganglion cells in the rabbit retina, none of which predominate numerically. So the question arises, what role do the LEDs play in fine spatial vision?

LEDs have complex receptive-field properties, which contrast with the simple bandpass properties of brisk-sustained X-cells. LEDs respond with sustained firing to stimulation of the receptive-field center by a light or dark spot but they are unresponsive to full-field stimuli, indicating that the LEDs have a strong inhibitory surround (Levick, 1967). The On and Off responses of LEDs are not symmetrical (Roska and Werblin, 2001), and when mapped with white-noise stimuli, LEDs appear to be essentially Off-center cells (DeVries and Baylor, 1997; Zeck et al., 2005). This is surprising given that the LEDs appear to stratify primarily in the On sublamina of the inner plexiform layer, but their location at the border of the On and Off sublaminas enables LEDs to receive input from both On and Off bipolar cells (Famiglietti, 2005a,b). LEDs are not confined to prey species like the rabbit, mouse, and guinea pig (Xu et al., 2005; Zeck et al., 2005; Berry, 2006; van Wyk, 2006), but are also present in predator species like the cat (Cleland and Levick, 1974; Berson et al., 1998), and may well be an integral component of the primate retina (Rodieck and Watanabe, 1993).

In his original study, Levick (1967) emphasized that LEDs detect contrast borders that are local to the receptive-field center, hence the name, but Roska and Werblin (2001) have shown that LEDs also respond to extended edges, like the brisk-sustained cells. Although the response properties of LEDs and brisk-sustained cells have been compared with emphasis on the spatial domain (Zeck et al., 2005), it is essential to also examine the behavior of LEDs in the temporal domain, where many of their complex properties become apparent.

Received May 10, 2006; revised Nov. 3, 2006; accepted Nov. 8, 2006.

This work was supported by National Health and Medical Research Council (Australia) Grant 351538 (D.I.V., N. S. Hart) and by National Eye Institute Grant EY014888 (W.R.T.).

Correspondence should be addressed to Prof. David I. Vaney, Vision, Touch and Hearing Research Centre, The University of Queensland, Brisbane, Queensland 4072, Australia. E-mail: d.vaney@uq.edu.au.

DOI:10.1523/JNEUROSCI.1991-06.2006

 0270-6474/06/2613250-14$15.00/0

Materials and Methods

Experiments were performed on adult pigmented rabbits of either sex. All reagents were obtained from Sigma (St. Louis, MO), unless otherwise indicated. Experiments conducted in Brisbane, Australia, were in accordance with the Australian Code of Practice and the protocols were approved by the Animal Ethics Committee at the University of Queensland, whereas experiments conducted in Portland, Oregon, were in accordance with National Institutes of Health guidelines, and the protocols were approved by the Institutional Animal Care Committee at Oregon Health & Science University.

Intracellular dye injection and histochemical labeling. The methods for intracellular dye injection of microscopically identified neurons in the isolated rabbit retina have been described in detail previously (Hampson et al., 1992). After anesthesia with ketamine (40 mg/kg) and xylazine (10 mg/kg), 0.4 mg of 4′,6-diamidino-2-phenylindole (DAPI) was injected into the vitreous (Masland et al., 1984), and 2 d later, the animal was administered a pentobarbitone overdose. The eyes were enucleated, hemisected, and the retina was separated from the underlying choroid. Isolated pieces of retina were mounted photoreceptor side down on black filter paper (AABG02500; Millipore, Bedford, MA) and superfused with carbogenated Ames medium at room temperature. The ganglion cell somata were vitally labeled with acridine orange, which produced a fluorescent Nissl-like staining in the perinuclear cytoplasm (Sandell and Masland, 1988; Dacey, 1989a; Vaney, 2004).

The sharp electrodes (~120 MΩ) were filled with either Alexa Fluor hydrazide (Alexa; 0.2% in water; Invitrogen, Eugene, OR) or a combination of Neurobiotin (4%; Vector Laboratories, Burlingame, CA) and Lucifer yellow (0.5%) in 0.1 M Tris buffer, pH 7.6. Alexa or Neurobiotin was iontophoresed into impaled cells for 1 min using −0.5 or +1 nA current, respectively. Tissue containing Neurobiotin-injected cells was incubated at 35°C for 30–120 min to allow diffusion of the tracer across gap junctions (Vaney, 1991). The retina was fixed for 40–60 min in freshly prepared 4% paraformaldehyde in 0.1 M PBS, pH 7.4. The Neurobiotin was visualized by incubating the retina overnight in 1:200 streptavidin–Alexa 488 (Invitrogen) and 0.5% Triton X-100 in PBS.

The dendritic morphology of dye-injected LEDs was reconstructed using confocal microscopy. A convex polygon was traced around the peripheral dendrites to delineate the dendritic field and the diameter calculated from a circle of equivalent area. The density of DAPI-labeled starburst amacrine cells overlapping each LED was measured and used to calculate the eccentricity from the visual streak, based on published density profiles of starburst cells (Masland et al., 1984; Vaney, 1984).

Amacrine cells containing GABA or glycine were labeled with antibodies provided by D. V. Pow (University of Newcastle, Newcastle, New South Wales, Australia) (Pow et al., 1995). The fixed tissue was incubated for 7 d at 4°C in a 1:400 primary antibody solution containing 0.5% Triton X-100, 2% bovine serum albumin (BSA), and 0.02% sodium azide in 0.1 M PBS. The tissue was subsequently washed for 30 min in 0.1 M PBS and incubated overnight in 1:200 Cy3-conjugated secondary antibody (Amersham Biosciences, Piscataway, NJ), 0.5% Triton X-100, and 2% BSA in 0.1% PBS. Amacrine cells containing nitric oxide synthase were labeled by NADPH–diaphorase histochemistry, by incubating fixed tissue for 30–120 min at 37°C in a reaction mixture containing 15 mM malic acid, 1 mM $MnCl_2$, 1 mM NADP, 0.2 mM nitroblue tetrazolium, and 0.2% Triton X-100 in 0.1 M Tris buffer, pH 8.2 (Sagar, 1986; Vaney and Young, 1988). Indoleamine-accumulating amacrine cells were labeled by incubating fresh retina at 37°C for 30 min in Ames medium containing 40 μg/ml of the fluorescent serotonin analog 5,7-dihydroxytryptamine (5,7-dHT) (Ehinger and Florén, 1976; Vaney, 1986).

Extracellular and patch-clamp recording. The methods for patch-clamp recording of the visually evoked currents in retinal ganglion cells have been described in detail previously (Taylor and Vaney, 2002). The rabbits were dark-adapted, and after pentobarbitone overdose, the eyes were enucleated under dim-red illumination and the retinas were removed. A piece of inferior retina was adhered photoreceptor side down to a cover glass coated with poly-L-lysine and then placed in a recording chamber perfused with Ames medium at 34–36°C, pH 7.4. The ganglion cells were targeted for recording using infrared differential interference contrast (IR-DIC) optics.

Extracellular and patch electrodes were pulled from borosilicate glass to a final resistance of 5–8 MΩ. The extracellular electrodes were filled with Ames medium, whereas the patch electrodes contained the following: 135 mM Cs-methylsulfonate, 6 mM CsCl, 2 mM Na-ATP, 1 mM Na-GTP, 1 mM EGTA, 2 mM MgCl, 5 mM Na-HEPES, and 5 mM lidocaine *N*-ethyl bromide (QX-314). Cesium was used in place of potassium to block voltage-gated potassium currents and thereby improve the quality of the voltage clamp at positive potentials. The QX-314 was included to block voltage-gated sodium channels and abolished all spiking activity within 1–2 min of establishing the whole-cell configuration. For whole-cell current-clamp recordings, potassium rather than cesium was used in the intracellular solution and the QX-314 was omitted. A liquid junction potential of –10 mV was subtracted from all voltages; there was no routine compensation for the series resistance. The chloride reversal potential, E_{Cl}, for these solutions was calculated to be approximately –54 mV, assuming that Br is 1.5 times more permeable that Cl through the inhibitory chloride channels (Bormann et al., 1987).

The conductance analysis methods have been described previously (Borg-Graham, 2001; Taylor and Vaney, 2002). Briefly, the light responses were recorded at holding potentials from –100 to +20 mV in 15 mV steps. The current–voltage relation (*IV*) for the net light-evoked current was measured at 5 or 10 ms intervals, and at each time point, a line was fitted to the *IV* curve between –85 and –25 mV (see Fig. 8*B*). The slope and the voltage axis intercept of the line provided measures of the light-evoked synaptic conductance (G_m) and the synaptic reversal potential (V_r), respectively. The excitatory component, G_e, and the inhibitory component, G_i, of the synaptic conductance can be calculated from G_m using V_r, which reflects the relative magnitudes of G_e and G_i. As $G_m \rightarrow 0$, the variance of V_r became very large because of noise in the data points. In the interests of clarity, V_r has been blanked-out in the figures when $G_m <$ 0.5 nS. It is also worth noting that, in some cases, V_r was more hyperpolarized than the calculated E_{Cl} (see Fig. 11), which resulted in negative excitatory conductance values. This could occur if a tonic excitatory conductance was shut off by the light stimulus. Although LEDs did display some tonic synaptic input (see Fig. 5*A*), the light-evoked synaptic inputs to these cells were clearly dominated by increases in conductance. A negative excitatory conductance could also be calculated if the actual E_{Cl} was more negative than the predicted value. In any case, such effects were too small and variable to analyze quantitatively and do not have a significant bearing on the results or conclusions.

The light stimuli were generated on a Macintosh computer monitor with a refresh rate of 85 Hz, using only the green gun of the cathode ray tube. The stimuli were projected through the microscope and focused onto the photoreceptor outer segments, via the 20× water immersion objective (numerical aperture, 0.95). The background light intensity (L_{BACK}) was set to 150 $\mu W/m^2$ at the retinal surface, which for the green phosphor of the stimulus monitor corresponds to ~400 photons $\cdot \mu m^{-2} \cdot s^{-1}$. Assuming a collecting area for the rabbit rods of ~1 μm^2, the background intensity was well above the scotopic range. The stimulus light intensity (L_{STIM}) was set to 30 $\mu W/m^2$ for dark stimuli and to 270 $\mu W/m^2$ for bright stimuli. Thus, the percentage stimulus contrast, defined as $C = 100 \times (L_{STIM} - L_{BACK})/L_{BACK}$, ranged from –80 to +80%.

The spatiotemporal white-noise stimuli comprised an 8 × 8 array of 40 μm squares. Stimulus frames were presented every 47.12 ms (21.22 Hz), which was one-quarter of the frame rate of the stimulus monitor. The reduced temporal bandwidth of the stimulus produced more vigorous responses in the sluggish LEDs. For each frame, each pixel was randomly assigned an intensity either higher ($p = 0.4$), lower ($p = 0.4$), or equal ($p = 0.2$) to the background intensity; the mean contrast was set to 64%. Six 30 s trials were applied and the spike-triggered average stimuli were accumulated from all trials to generate the results shown in Figure 7. The time course of the spike-triggered average stimulus was calculated from the pixels within the receptive-field center, which was defined as the area in which the spike-triggered average intensity exceeded the background variance by 2 SDs, 150 ms before the spike (see Fig. 7*C*). The receptive-field size was calculated using a least-squares minimization

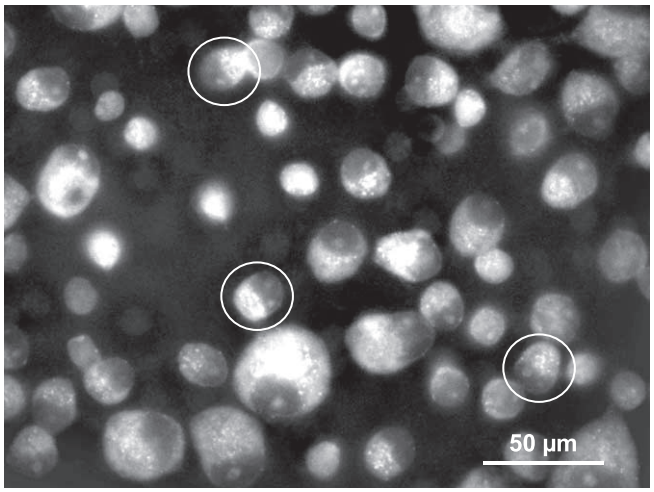

Figure 1. Microscopic identification of LED somata. Shown is a fluorescence micrograph of a piece of rabbit retina labeled with acridine orange, with the focus on the ganglion cell layer; this field was located 1 mm ventral to the visual streak. Presumptive LEDs (circles) can be identified by the size and shape of the soma and nucleus.

routine (Igor Pro; Wavemetrics, Lake Oswego, OR) to fit a two-dimensional Gaussian to this image according to the following equation:

$$z = z_0 + z_{\max} \exp\left[-\frac{1}{2}\left(\left(\frac{(x - x_0)\cos\theta - (y - y_0)\sin\theta}{\sigma_x}\right)^2 + \left(\frac{(x - x_0)\sin\theta + (y - y_0)\cos\theta}{\sigma_y}\right)^2\right)\right],$$

where z is the pixel intensity, z_0 is the baseline offset, $z_{\max}$ is the peak intensity, (x_0, y_0) is the location of the peak, σ_x and σ_y are the widths along the long and short axes of the Gaussian, and θ is the orientation of the long axis. For all the fits, z_0 was not significantly different from zero.

Results

Cell identification and dendritic morphology

The LEDs were targeted microscopically on the basis of their distinctive somatic appearance. In whole-mount retinas labeled with acridine orange, which produced a fluorescent Nissl-like staining of the cytoplasm, the somata of LEDs were ~12 μm in diameter, which is smaller than most ganglion cell somata in the rabbit retina. The semicircular nucleus of LEDs was offset to one side of the soma and occupied about one-half of the cytoplasmic volume (Fig. 1, circle). With practice, the LEDs could be selected for intracellular injection under direct microscopic control with a success rate approaching 70% in peripheral retina; the LEDs were much harder to identify in the visual streak, where the somata of ganglion cells are smaller and more uniform in appearance.

The injection of Lucifer yellow, Alexa Fluor hydrazide, or Neurobiotin into LEDs revealed their characteristic dendritic morphology, which matched that previously described in the rabbit retina (Amthor et al., 1989; Roska and Werblin, 2001; Rockhill et al., 2002; Famiglietti, 2005b). The small soma gave rise to a correspondingly thin axon, as expected for a ganglion cell type with a slow conduction velocity (Caldwell and Daw, 1978; Vaney et al., 1981). The LEDs had a highly branched dendritic tree containing numerous terminal dendrites; most of the dendrites stratified in the middle of the inner plexiform layer (stratum 3), but some dendrites extended a few micrometers more distally toward stratum 2 (Fig. 2*A*,*B*). The stratification level could be visualized by injecting one dye into an LED and a different dye into an overlapping On–Off direction-selective ganglion cell (DSGC), whose bistratified dendrites branched at 20 and 70% depth of the inner plexiform layer, where 0% depth corresponds to the border of the inner nuclear and inner plexiform layers. Such preparations showed that LEDs stratify between the On and Off strata of the DSGC, at ~45% depth of the inner plexiform layer (Fig. 2*C*,*D*).

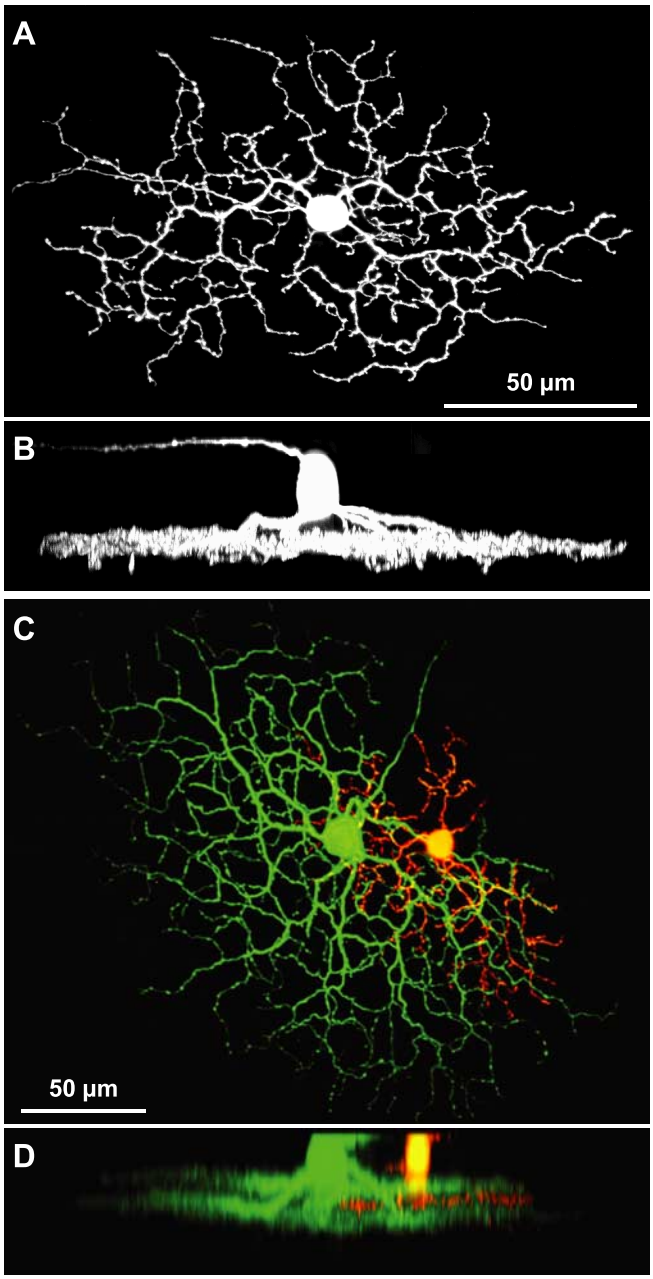

Figure 2. Dendritic morphology and stratification of LEDs. ***A***, Through-projection of an Alexa 488-injected LED reconstructed from 29 confocal micrographs. ***B***, Side projection of the same cell. ***C***, Through-projection of an Alexa 568-injected LED with an overlapping Alexa 488-injected On–Off direction-selective ganglion cell. ***D***, Side projection of the same cells; the monostratified dendrites of the LED are sandwiched between the bistratified dendrites of the direction-selective cell. The vertical dimension in ***B*** and ***D*** has been stretched for illustration purposes.

To determine how the dendritic-field size of the LEDs varied with retinal eccentricity, 23 cells were injected with dye and photographed; a convex polygon was then traced around the distal dendritic tips, and the dendritic-field area was measured. LEDs were encountered at all eccentricities and showed a 20-fold increase in dendritic-field area from central retina to the far periph-

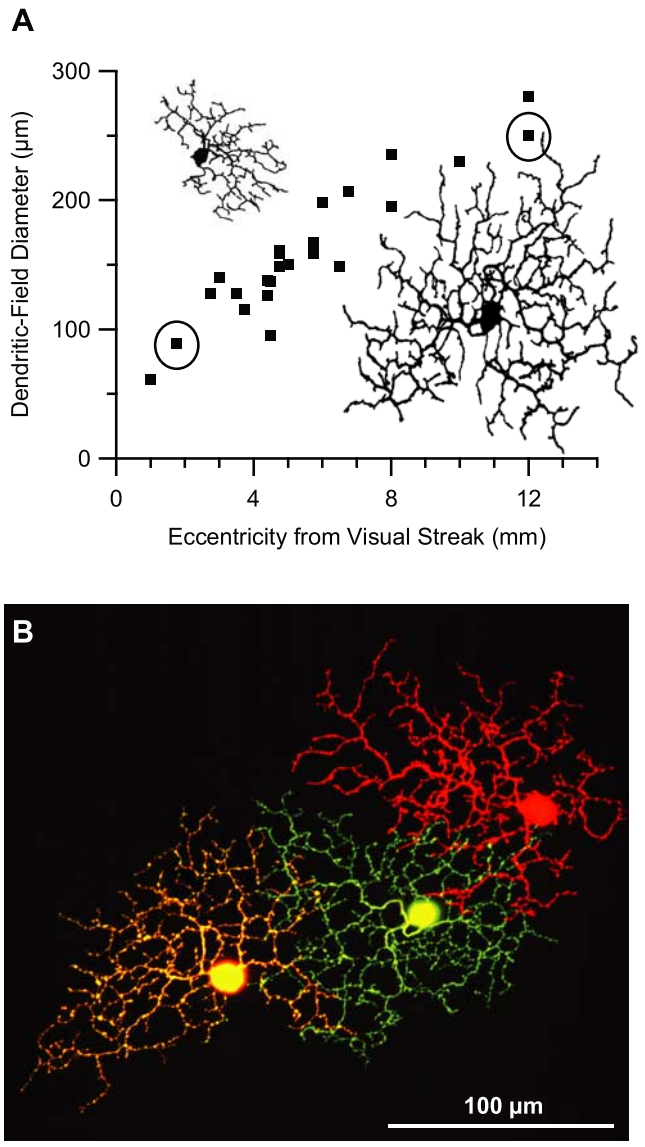

Figure 3. Retinal topography of LEDs. ***A***, Dendritic-field size of Neurobiotin-injected cells increased as the ganglion cell density declined with retinal eccentricity from the visual streak; the circles mark one cell near the streak and another in the far periphery whose dendritic morphology is shown in the inset drawings, scaled relative to the vertical axis of the graph. ***B***, Confocal reconstruction of three adjacent LEDs injected with Alexa Fluor dyes (green, Alexa 488; red, Alexa 568; yellow, Alexa 488 and Alexa 568) shows that they overlap substantially, with the dendrites of each cell reaching almost as far as the soma of the neighbors.

ery: one cell located within 1 mm of the peak visual streak had an equivalent diameter of 60 μm, whereas two cells located 12 mm ventral from the streak had equivalent diameters of 250 and 280 μm (Fig. 3*A*). In another experiment, just the ganglion cells in the peak visual streak were targeted and the 10 injected LEDs that had the smallest dendritic fields ranged in size from 49 to 68 μm equivalent diameter (mean, 62 $\pm$ 7 μm). The dendritic-field diameters of LEDs were comparable with those reported in previous studies of central rabbit retina [~80 μm (Amthor et al., 1989); 50–150 μm (Famiglietti, 2005b)] and midperipheral retina [150–200 μm (Rockhill et al., 2002)].

Dendritic-field overlap and cell density

To examine the dendritic-field overlap of LEDs, two or three neighboring cells were injected with different fluorescent dyes (Fig. 3*B*). Confirmation that such pairs or triplets of cells comprised a single morphological type was provided by (1) the uniform dendritic morphology, (2) the minimal local variation in dendritic-field size, and (3) the precise costratification of the dendrites. This enabled us to exclude from consideration the G2 ganglion cells, which have a more open dendritic morphology, larger dendritic fields, and stratify at ~55% depth of the inner plexiform layer (Rockhill et al., 2002). In the dual- and triple-labeled preparations, it was apparent that the dendritic trees of neighboring LEDs partially overlapped, with the dendrites of one cell usually stopping a little short of the soma of the adjacent cell. This is shown in Figure 3*B* for three neighboring LEDs located ~3 mm ventral to the peak visual streak; the dendritic-field organization of LEDs within the visual streak was qualitatively similar.

Such dendritic-field overlap, with the somatic spacing being about one-half of the dendritic-field diameter, is shown by other types of ganglion cells (Koch et al., 2006), including the α-cells, β-cells, and monoamine-accumulating ganglion cells of the cat retina (Wässle et al., 1981; Dacey, 1989b). In contrast, the direction-selective ganglion cells of the rabbit retina and the midget ganglion cells of the primate retina show a territorial dendritic-field organization, with restricted dendritic-field overlap (Buhl and Peichl, 1986; Dacey, 1993; Vaney, 1994; Amthor and Oyster, 1995).

The dendritic-field overlap of the LEDs was calculated by multiplying the dendritic-field area by the local cell density, which was derived by assuming that the LED somata approximate a regular square array: for somata separated by x mm, the density would be $1/x^2$ cells/mm^2. (Regular hexagonal packing of the somata would increase the density by a factor of $2/\sqrt{3}$ or 1.15-fold.) The mean somatic spacing of the three LEDs in Figure 3*B* is 80 μm, indicating that the local density of LEDs is ~156 cells/mm^2; the mean dendritic-field area of the three LEDs is 0.0133 mm^2, giving a 2.1-fold dendritic-field overlap. The density of all ganglion cells located 3 mm ventral to the visual streak is ~1000 cells/mm^2 (Provis, 1979; Vaney, 1980b; Oyster et al., 1981), indicating that the LEDs account for ~16% of the ganglion cells at this retinal eccentricity. Another triplet of LEDs located ~1 mm ventral to the peak visual streak had a mean dendritic-field diameter of 72 μm and a mean somal separation of 46 μm, indicating a density of 475 cells/mm^2 and a 1.9-fold dendritic-field overlap.

If the smallest LEDs in the peak visual streak also have a two-fold dendritic-field overlap, then their intercellular spacing can be calculated simply from the dendritic-field size: a diameter of 62 $\pm$ 7 μm would produce a somal separation of 39 $\pm$ 5 μm. The actual spacing may be near the lower end of this range because one pair of dye-injected LEDs in the peak visual streak was separated by only 28 μm spacing and another pair recorded near the peak visual streak had a center-to-center spacing of 34 μm (see below, Spatial response properties). A square array of LEDs with a spacing of 39 $\pm$ 5 μm would have a density of 550–850 cells/mm^2, which would account for 11–17% of the 5000 ganglion cells/mm^2 in the peak visual streak (Provis, 1979; Vaney, 1980b; Oyster et al., 1981).

To provide an independent estimate of the proportion of LEDs in the visual streak, ganglion cells located ~250 μm ventral of the peak visual streak were randomly selected for dye injection by moving the microscope stage an arbitrary distance and then targeting the ganglion cell located in the center of the oculars. Seven of the 49 ganglion cells recovered had the distinctive dendritic morphology of LEDs, and they had smaller dendritic trees

than any of the other 42 ganglion cells injected with dye. This 14% encounter rate probably underestimates the true proportion of LEDs, because ganglion cells with larger somata would be oversampled.

Thus, several lines of evidence from this study indicate that the LEDs account for ~15% of the ganglion cells in the rabbit retina. In agreement with this conclusion, Rockhill et al. (2002) estimated that the LEDs account for 18% of the ganglion cells in peripheral rabbit retina, based on the assumptions that the cell density of each ganglion cell type is proportional to the inverse of dendritic-field area, and that all types show the same dendritic-field overlap. In contrast, Famiglietti (2005b) estimated that the LEDs account for only 7% of the ganglion cells in the rabbit retina; however, his figure was based on the untested assumption that the dendritic fields have only a 1.2-fold overlap, rather than the twofold overlap measured in this study. In fact, similar to this study, Famiglietti's micrographs of pairs of Golgi-stained LEDs show that the dendrites of each LED extend well into the dendritic field of the neighboring LED, supporting our conclusion that the LEDs have a twofold dendritic-field overlap.

Tracer-coupling pattern

LEDs injected with Neurobiotin, which is a gap-junction permeable tracer (Vaney, 1991), showed no homologous tracer coupling to neighboring LEDs but consistently showed heterologous tracer coupling to two types of amacrine cells. The LED in Figure 4*A* shows strong tracer coupling to three wide-field amacrine cells, whose slender varicose dendrites stratify in the same plane as the LED. The soma of one cell is located within the dendritic field of the LED, whereas the second soma is located on the edge of the dendritic field and the third soma is located beyond the dendritic field. Regardless of soma position, the dendritic tree of each of the wide-field amacrine cells completely overlaps the small dendritic tree of the LED, providing many points of close apposition where gap junctions could be located. The somata of the wide-field tracer-coupled cells were weakly immunopositive for GABA (Fig. 4*B*) and immunonegative for glycine (Fig. 4*C*) and glycine transporter 1, indicating that they are GABAergic, like most types of wide-field unistratified amacrine cells (Vaney, 2003).

Although the morphology and stratification level of the wide-field tracer-coupled cells resembled those of the wide S3 amacrine cells, which accumulate 5,7-dHT weakly (Vaney, 1986, 1990), double labeling established that they are different cell types (data not shown). Moreover, NADPH-diaphorase histochemistry showed that the wide-field tracer-coupled cells do not correspond to the type 1 or type 2 nitrergic amacrine cells, both of which also contain GABA and branch in stratum 3 (Vaney and Young, 1988). Clearly, there are more types of stratified amacrine cells that are well positioned to provide synaptic input to the LEDs than are recognized by current classification schemes (MacNeil et al., 1999).

The Neurobiotin-injected LED in Figure 4*A* shows tracer coupling to a fourth amacrine cell, whose soma is smaller than that of the three tracer-coupled wide-field cells. Such somata were immunopositive for glycine (Fig. 4*C*) and immunonegative for GABA (Fig. 4*B*), indicating that they are glycinergic amacrine cells. Although the weakly labeled processes of these cells could not be traced, most glycinergic amacrine cells are narrow-field neurons (Vaney, 2003), and this explains why the glycine-immunopositive tracer-coupled somata were mostly confined to the dendritic field of the LED, whereas the GABA-immunopositive tracer-coupled somata were usually located beyond the dendritic field of the LED. There are numerous types of glycinergic amacrine cells in the mammalian retina, many of which overlap stratum 3 of the inner plexiform layer (Pourcho and Goebel, 1985; Menger et al., 1998). The narrow S3 amacrine cell is an obvious candidate (MacNeil et al., 1999) but the only type that could positively be excluded was the AII amacrine cell, which is only weakly immunopositive for glycine (Vaney et al., 1998).

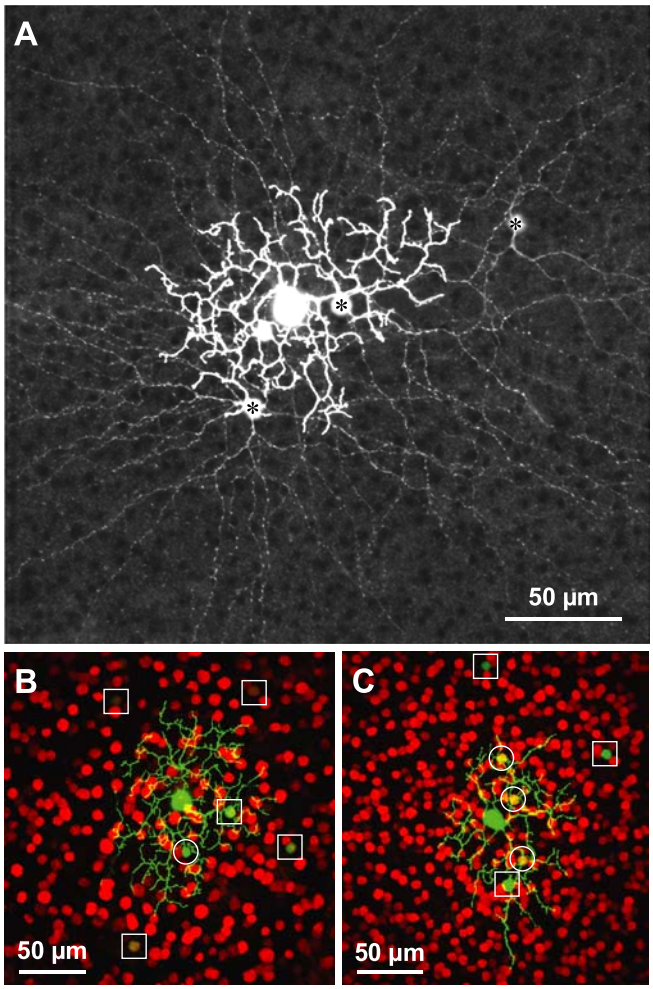

Figure 4. Tracer-coupling pattern of LEDs. ***A***, Confocal reconstruction of a Neurobiotin-injected LED reacted with Alexa 488–streptavidin shows that the LED is tracer-coupled to four overlapping amacrine cells, three of which have wide-field unistratified dendritic trees (asterisks). ***B***, Confocal reconstruction of a Neurobiotin-injected LED (green) and the corresponding field of GABA-immunoreactive amacrine cells (red); five tracer-coupled somata that are weakly GABA-immunopositive are located within and external to the LED dendritic field (squares), whereas a single tracer-coupled soma that is GABA-immunonegative is located within the dendritic field (circle). ***C***, Confocal reconstruction of a Neurobiotin-injected LED (green) and the corresponding field of glycine-immunoreactive amacrine cells; three tracer-coupled somata that are strongly glycine-immunopositive are located within the LED dendritic field (circles), whereas three tracer-coupled somata that are glycine-immunonegative are located within and external to the dendritic field (squares).

Receptive-field properties

LEDs were targeted for electrophysiological recording based on the soma size and the shape of the nucleus, as viewed under IR-DIC optics. Six of these cells were injected with dye, thus confirming that they had the same dendritic morphology as the numerous LEDs studied by anatomical methods alone. However, the cells were not routinely injected after recording experiments,

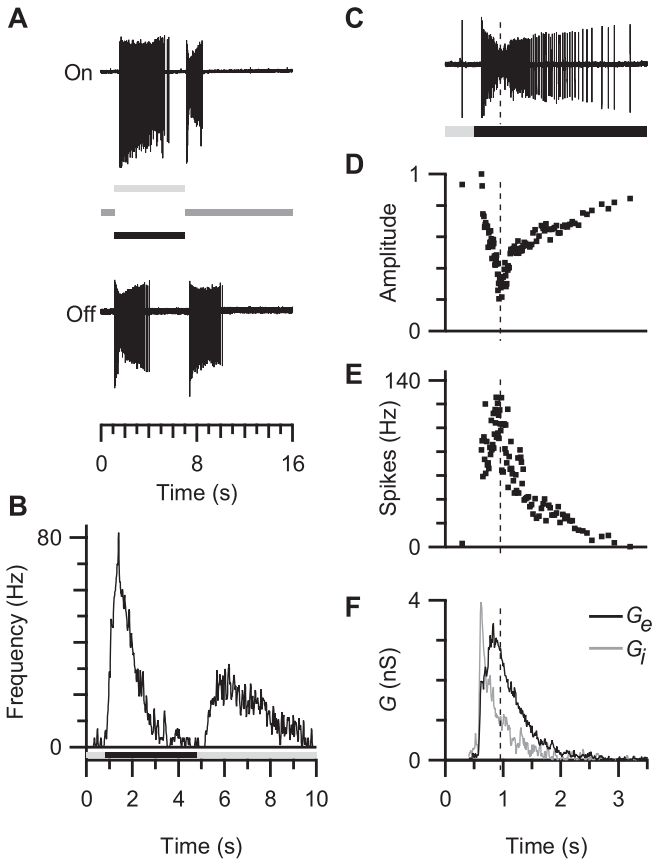

Figure 5. On–Off responses of LEDs. ***A***, When a bright or dark spot of 100 μm diameter was presented for 6 s, LEDs produced sustained firing for several seconds at both the initiation and termination of the stimulus. ***B***, Spike-time histogram for stimulation by a dark spot, accumulated from six LEDs; the ordinate shows equivalent spike-rate per trial for 10 ms bins. ***C***, Spike responses recorded at the initiation of a dark-spot stimulus. ***D***, The relative amplitude of the extracellular spikes was strongly attenuated ~0.5 s after stimulus initiation. ***E***, Peak attenuation of the spike amplitude coincided with the maximum spike rate during the response. ***F***, Synaptic conductances observed in the same cell during the light stimulus.

and instead, the following simple physiological criteria were used to identify LEDs from extracellular recordings. (1) The cell gave both On and Off responses to light or dark spots flashed in the receptive-field center (Fig. 5*A*,*B*). (2) Relatively small spots of ~100 μm diameter elicited the strongest response (Fig. 6*B*). (3) The spike train had a characteristic hourglass shape, with the spikes being smallest ~0.5–1 s after stimulus initiation (Fig. 5*C*). It is likely that the attenuation of the spike amplitude was partly attributable to sodium channel inactivation at high discharge rates given that the degree of attenuation closely mirrored the interspike interval during the response (Fig. 5*D*,*E*). The mean depolarization produced by the excitatory input to the cell might also have contributed to sodium channel inactivation, because the spike amplitude attenuation also correlated well with the time course of the excitatory synaptic conductance (Fig. 5*F*).

Measurements taken from five LEDs under current clamp showed that the mean resting potential was –80.8 ± 1.9 mV, the membrane time constant was 19.6 ± 7.2 ms, and the input resistance was 180 ± 17 MΩ. During whole-cell current-clamp recordings, spikes rapidly became attenuated and eventually disappeared entirely, presumably because of the loss of intracellular constituents to the patch electrode (data not shown). In contrast, spikes recorded from other types of ganglion cells, using essentially identical intracellular solutions, were stable for similar recording periods (Velte and Masland, 1999; Oesch et al., 2005). The reasons for the labile nature of LED spiking were not investigated further, but all analysis that required measurement of spiking activity was performed using extracellular recordings.

Early extracellular-recording studies of the receptive-field properties of LEDs, using spot and edge stimuli, indicated that the LEDs are sustained On–Off cells that respond to local changes in contrast, regardless of sign (Levick, 1967; Cleland and Levick, 1974; Caldwell et al., 1978). By comparison, more recent studies of spike discharge using spatiotemporal white-noise stimuli have indicated that LEDs are sluggishly responding Off-center cells (DeVries and Baylor, 1997; Xu et al., 2005; Zeck et al., 2005; Berry, 2006). In the following sections, we examine the spatial and temporal properties of LED receptive fields and show how an analysis of the underlying excitatory and inhibitory synaptic inputs can resolve these differing viewpoints.

Spatial response properties

Area–response measurements were used to map the spatial extent of the LED receptive field. The Off response first appeared for a dark spot stimulus of 20–50 μm diameter. The number of spikes increased with spot size, reached a maximum at 100–200 μm, and then declined with additional increases in spot size (Fig. 6*A*). The peak response was associated with the minimum latency to the first spike, which occurred ~150 ms after stimulus initiation. The area–response curve for the Off response was well described by a difference of Gaussians (DOG) function (Fig. 6*B*) and was thus typical of concentric center-surround receptive fields (Rodieck and Stone, 1965). The mean center diameter at 1 SD was 145 ± 7 μm and the mean surround diameter was 642 ± 42 μm, with the largest stimuli suppressing the response to 27% of the maximum.

The area–response function for the On response, measured when the dark spot was extinguished, was qualitatively different from the area–response function for the Off response. Small spot stimuli that produced a robust Off response failed to produce any On response, with the first On response only being elicited by stimuli of 50–100 μm diameter. The On response then increased rapidly with spot diameter, so that the optimal stimulus size for the On response was about the same as that for the Off response (Fig. 6*B*). However, the On response was more strongly inhibited than the Off response by additional increases in stimulus size and the largest spots generally produced complete suppression of the On response. Moreover, the abrupt increase in the On response between the threshold and maximal levels was poorly predicted by a DOG function. Together, these results suggested that there are marked differences in the circuitry underlying the On and Off responses, a contention that is borne out by subsequent analysis of the temporal response properties.

The relationship between receptive-field and dendritic-field size was examined for six LEDs that were injected with dye after their area–response functions had been measured (Fig. 6*C*). The size of the Off-center, as calculated from the DOG function, increased monotonically with dendritic-field diameter, with the line of best fit through the origin having a slope of 1.4. Consequently, at each eccentricity, the receptive-field area was approximately twofold larger than the dendritic-field area, probably because of the convergence of bipolar cells onto the LEDs. When this figure is multiplied by the previously calculated twofold dendritic-field overlap, it indicates that the LEDs have a fourfold receptive-field overlap.

The extent of receptive-field overlap was confirmed directly by mapping the receptive fields of two pairs of neighboring LEDs,

whose extracellular responses were recorded simultaneously in response to a pseudorandom checkerboard stimulus updated at 21.2 Hz. The spike-triggered average stimulus, which was calculated at equal multiples of the stimulus period up to 1 s before the spike, indicated that the LEDs were Off-center cells (Fig. 7*A*), consistent with previous reports (DeVries and Baylor, 1997; Xu et al., 2005; Zeck et al., 2005; Berry, 2006). The linear kernels were very similar in four cells, which comprised two pairs near the visual streak in a single preparation. The spike-triggered average stimuli were initially lighter than background and then became much darker, reaching minimum intensity ~150 ms before the spike (Fig. 7*B*).

The extent of the receptive-field center was determined by fitting a two-dimensional Gaussian function to the average image obtained 150 ms before the spike, corresponding to the peak Off modulation. Contour plots for the illustrated cell pair show that the receptive fields overlapped significantly at the 1 SD level, with the edge of each receptive field reaching almost as far as the center of the neighboring receptive field (Fig. 7*C*,*D*). The center-to-center distance was 34 μm and the receptive-field widths at 1 SD were 66 and 60 μm, giving a 2.7- to 3.1-fold receptive-field overlap, with the two extremes corresponding to regular square- and hexagonal-packing of the cells, respectively. Both the checkerboard results and the area–response analysis (Fig. 6*C*) indicated that there was multiple overlap of the Gaussian centers of the LED receptive fields, when measured at the 1 SD level, although the fourfold overlap predicted from the area–response function was slightly greater than the threefold overlap apparent from the paired-cell recordings.

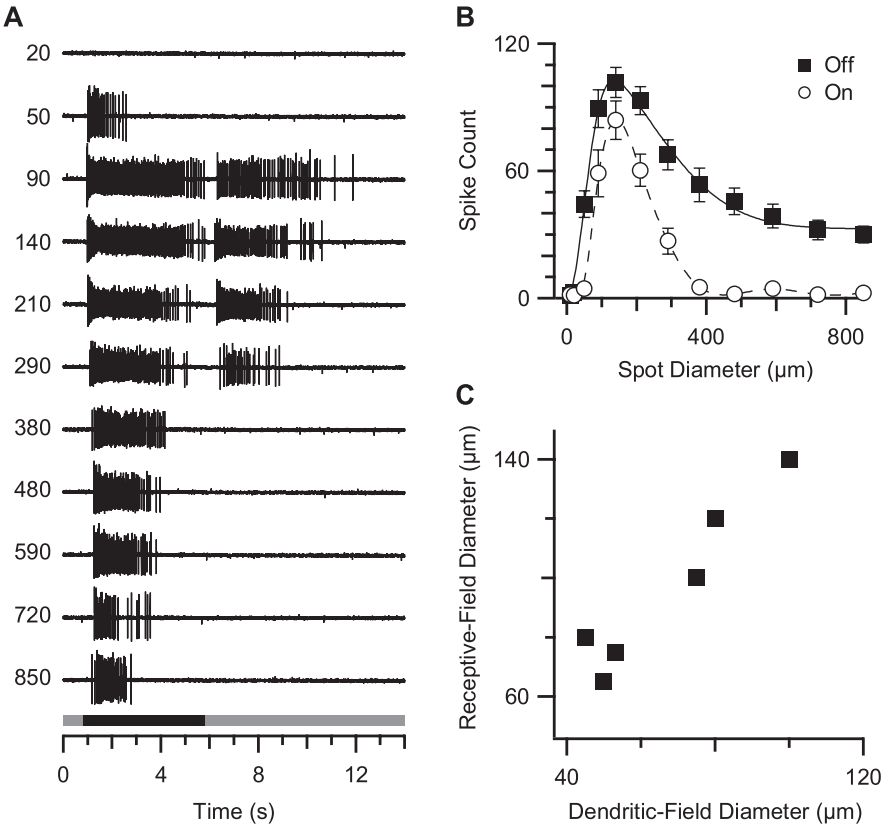

Figure 6. Spatial response properties of LEDs. ***A***, Spike responses of an LED to dark spots of increasing diameter (size in micrometers) presented for 5 s (black bar). Off responses were elicited by a broad range of spot sizes, whereas On responses appeared only when spots had a similar size to the receptive-field center. ***B***, Area–response function for 10 LEDs, showing the mean spike count (±SEM) for dark spots of increasing diameter. The smooth curve through the Off-response data (black squares) shows the best-fitting DOG function (see Materials and Methods); parameters were as follows: $A_c = 121 \pm 6$ spikes, $\sigma_c = 72 \pm 4$ μm, $A_s = 88 \pm 5$ spikes, and $\sigma_s = 321 \pm 21$ μm. The dashed curve through the On response data (white circles) shows a smooth interpolation of the data points. ***C***, Comparison of receptive-field and dendritic-field diameters for six Neurobiotin-injected LEDs; the receptive-field diameters were determined from fits to DOG functions, as shown in ***B***.

DeVries and Baylor (1997) used similar checkerboard stimuli with their multielectrode array (MEA) recordings and calculated that the receptive fields of neighboring LEDs touched at their 1 SD contours, whereas we found that the 1 SD contour of each LED extended almost as far as the center of the neighboring LED. The reason for this difference is not clear. DeVries and Baylor's recordings were made 1–5 mm below the visual streak, where we would expect the LEDs to be spaced ~50–90 μm apart. In Figure 6*E* of the study by DeVries and Baylor (1997), the closest LEDs are separated by ~100 μm, raising the question of whether the 70 μm spacing of their MEA undersampled the mosaic of LEDs. In contrast, a more recent MEA study of the ganglion cells in the guinea pig retina reported that the LEDs showed about a fourfold receptive-field overlap (Berry, 2006), in agreement with the findings of this study.

Synaptic mechanism of surround inhibition

Both the Off-center and On-center responses were inhibited by stimuli that extended beyond the central excitatory receptive field, with the suppression of the Off responses being incomplete generally and the suppression of the On responses being complete (Fig. 6*B*). It was not clear whether the surround suppressed spiking by directly inhibiting the LED or whether it acted indirectly by inhibiting the excitatory drive from bipolar cells. To determine the mode of suppression, we made patch-clamp recordings from LEDs and directly measured the excitatory and inhibitory synaptic conductances that were elicited by center or center-plus-surround stimulation.

Center stimulation, using a 100 μm diameter dark spot, elicited strong excitatory and inhibitory conductances for both negative and positive contrasts (negative contrast: Fig. 8*A–D*, left panels). The synaptic inputs activated rapidly, compared with the delay to the first spike. Measurements from eight cells produced an average time to half-peak of 70 ± 6 ms for the Off response, and 72 ± 5 ms for the On response; the corresponding spike delays to half-peak were 220 and 480 ms, respectively (Fig. 5*B*). Although the synaptic delays were very similar for the On and Off responses, the spike delays differed by more than twofold.

The different spike delays for the On and Off responses can be explained by the magnitude and trajectory of the synaptic conductances and their effects on the synaptic reversal potential, V_r. At both the initiation (Off response) and termination (On response) of the stimulus, V_r depolarized from about −40 to −10 mV (Fig. 8*C*, left). This positive shift was more rapid for the Off response than the On response, mainly because of the different kinetics of the excitatory inputs. The On excitation was slower to

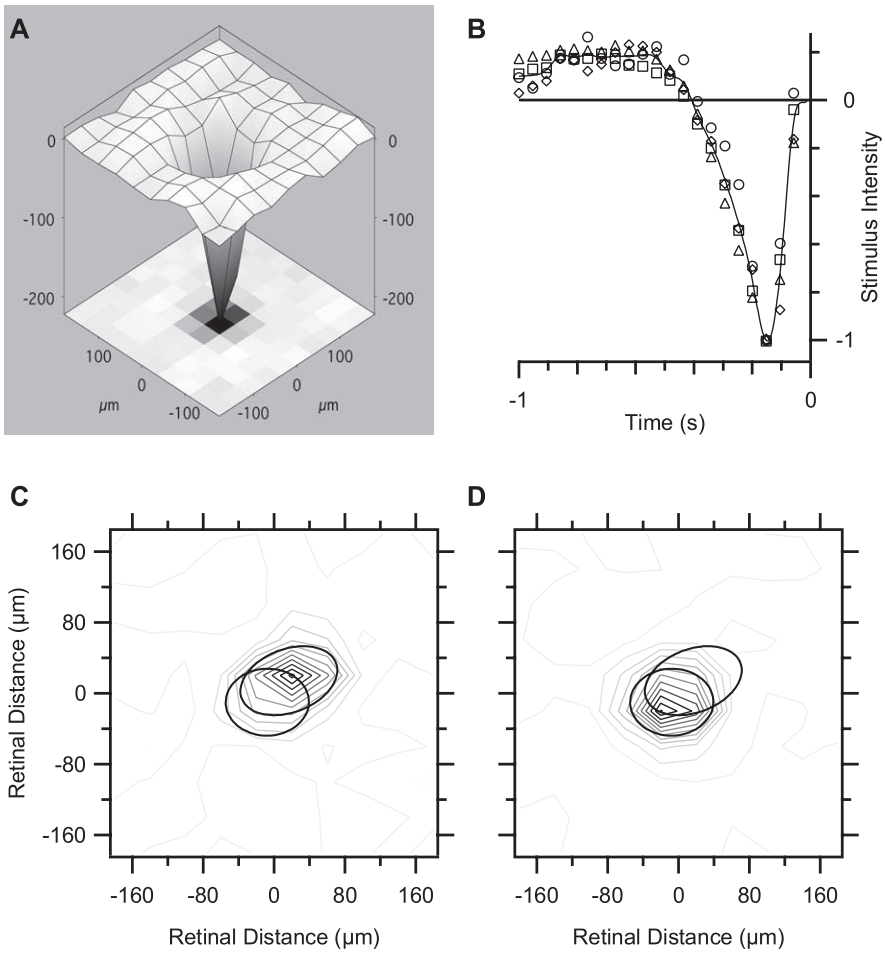

Figure 7. Receptive-field overlap determined from a spatiotemporal white-noise stimulus. ***A***, Spike-triggered average stimulus for one LED obtained 150 ms before the spike; stimulus pixel size was 40 μm, display rate was 21.2 Hz. ***B***, Time course for four LEDs (different symbols) of the intensity of the central pixels from the spike-triggered average stimulus, normalized to the response amplitude at −150 ms; the smooth curve shows a cubic interpolation. ***C***, ***D***, Contour plots of the peak spike-triggered average stimulus in two adjacent LEDs, which were recorded simultaneously, showing the extent of receptive-field overlap; the contour plots for each cell are plotted separately for clarity. The smooth ellipses show the 1 SD contour of the best-fitting Gaussian surface for both the plotted cell and the adjacent cell: the 1 SD contour of each LED reaches the center of the adjacent cell.

activate than the Off excitation (Fig. 8*E*, thick green lines); in contrast, the kinetics of the inhibitory inputs were faster and more similar for the On and Off responses (Fig. 8*E*, thick red lines). However, the Off inhibition displayed an initial rapid decline, not evident for the On inhibition, and this might also contribute to the shorter spike latency for the Off responses.

Center-plus-surround stimulation, using an 850 μm diameter dark spot, elicited much smaller excitatory and inhibitory conductances for both the Off and On responses (Fig. 8*A–D*, right panels), indicating that the surround inhibition acts presynaptically on both the excitatory bipolar cell inputs and the inhibitory amacrine cell inputs. Closer examination revealed differences between the Off and On responses. The On excitation was more strongly suppressed than the Off excitation (Fig. 8*E*, top panels). Surround stimulation strongly suppressed the sustained inhibition but spared the initial transient component (Fig. 8*E*, bottom panels). The initial peak of the inhibitory inputs was relatively unaffected by surround stimulation for the On response but was suppressed by ~40% for the Off response. Overall, the results indicate that postsynaptic integration plays little or no role in generating the suppressive effects of the surround in LEDs.

In his original definitive study, Levick (1967) suggested that the LEDs were inhibited most strongly when the surround contained edges. This idea was tested by examining whether surrounds composed of square-wave gratings produced stronger inhibition than a uniform surround stimulus (Fig. 9). The surrounds were static and presented simultaneously with the center stimulation. Although the uniform surround stimulus consistently produced the strongest inhibition, a low spatial-frequency grating covering the same area also caused strong inhibition, although it produced only one-half of the mean luminance change. This suggested that the strength of the surround inhibition may depend on several factors, including total luminance and the presence of edges. Additional support for this idea was obtained by increasing the spatial frequency of the surround grating, while maintaining the same mean luminance change. As the spatial frequency of the grating in the surround increased, the inhibition became progressively less effective, and at the highest frequency tested, surround stimulation produced very little inhibition. Because the mean luminance of the surround remained invariant as the spatial frequency was increased, these results suggest that surround inhibition is strongest when the surround mechanism can resolve edges, in agreement with Levick's findings.

Temporal response properties

As noted above, the delay before spike initiation observed for flash stimuli appeared to reflect rapidly activating inhibition coupled with slowly activating excitation (Fig. 8*D*,*E*). The peristimulus time histograms (Fig. 5*B*) and the analysis of synaptic conductance (Fig. 8) underscore the marked differences in the temporal properties between the On and Off responses.

We extended the analysis of the temporal response properties using sinusoidal modulation of optimally sized spots centered on the receptive field. At the lowest frequency tested (0.125 Hz), the extracellular spike responses were frequency doubled, as the cell responded during both the light and dark phases of modulation (Fig. 10*A*). Peristimulus time histograms combined from trials in 10 cells revealed peak firing rates of ~100 Hz (Fig. 10*B*). The On response was weaker than the Off response, and >0.25 Hz, the On spikes were no longer apparent, whereas the Off spikes were elicited up to 1–2 Hz. The sluggish responses shown by LEDs contrasted with the relatively brisk responses shown by other types of retinal ganglion cells, which responded well to frequencies >1 Hz (Fig. 10*C*).

To determine the synaptic basis for the sluggish spiking of LEDs, we measured the synaptic conductances elicited by the same sinusoidally modulated stimuli (Fig. 11). Inspection of the conductance records showed that the inhibitory component was strongly modulated up to the highest frequency tested, whereas the excitatory component became relatively more attenuated. This is most easily appreciated by considering the synaptic rever-

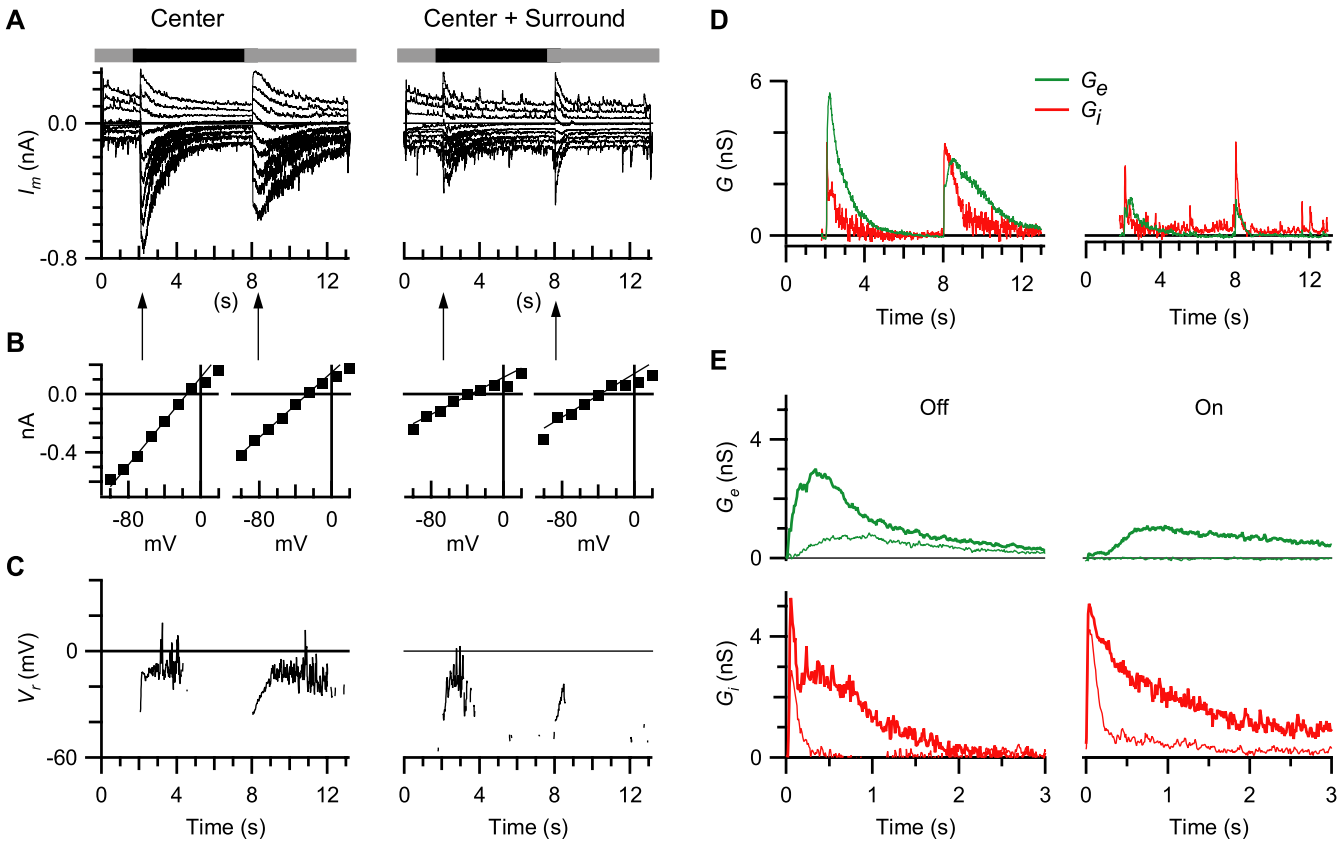

Figure 8. Synaptic mechanisms generating surround inhibition. ***A***, Synaptic currents, I_m, elicited by center stimulation (100 μm diameter dark spot) and center-plus-surround stimulation (850 μm diameter dark spot) at a series of holding potentials from −100 to +20 mV in 15 mV steps; the stimulus timing and contrast sign are shown by the bars above the current records. ***B***, Examples of the *IV* relations measured at the time points indicated by the arrows. The regression lines through the measurements demonstrate that the synaptic conductances were linear over the expected physiological voltage range; the slope and voltage axis intercept of the regression lines were used to evaluate the synaptic conductance and synaptic reversal potential, respectively. ***C***, Synaptic reversal potential, V_r, calculated for the currents shown in ***A***; for clarity, the reversal potential is only displayed when the synaptic conductance exceeded 0.5 nS. ***D***, Synaptic conductances calculated for the currents shown in ***A***; the excitatory (G_e; green) and inhibitory (G_i; red) components were derived as described in Materials and Methods. ***E***, Excitatory and inhibitory conductance components for center (thick lines) and center-plus-surround (thin lines) stimulation; each record is an average from four LEDs.

sal potential, V_r, which is determined by the ratio of excitation to inhibition. At low temporal frequencies, V_r is strongly modulated and reaches depolarizing levels approaching 0 mV. At high frequencies, V_r is only weakly modulated and, for the most part, remains below –50 mV. Thus, the sluggish spiking characteristics of LEDs can be attributed to the higher temporal response properties of inhibition relative to excitation. It is also worth noting that V_r displayed a transient positive excursion at 2 and 4 Hz (Fig. 11*E*,*F*), which underlies the tendency for LEDs to fire spikes only during the first stimulus cycle at higher frequencies (Fig. 10*A*,*B*). This can be explained by two factors: (1) the Off excitation is invariably larger during the first stimulus cycle; (2) inhibition is smaller at the onset of the stimulus and is larger during subsequent cycles, particularly at the higher frequencies.

A marked difference between the On and Off conductances is manifest in the loss of On spikes at relatively low stimulus frequencies. At the lowest frequency (0.125 Hz), the V_r trajectory is depolarizing during both the dark and light phases of the stimulus (Fig. 11*A*), and such frequency doubling is consistent with the spike recordings (Fig. 10*A*,*B*). At 0.25 Hz, the frequency doubling is much weaker because of the decline of the excitatory On response (Fig. 11*B*); >0.25 Hz, the On excitation disappears, frequency doubling vanishes, and the excitatory inputs are dominated by Off responses (Fig. 11*C*–*E*). In contrast, the inhibitory inputs demonstrate frequency doubling at all frequencies. Figure 11 shows these characteristics for a single cell that was tested at all frequencies, and this behavior was confirmed in other cells tested with subsets of the frequencies.

A simple model that might explain the temporal characteristics assumes that the excitatory and inhibitory inputs are generated independently and then summed postsynaptically within the LED. Moreover, it is most straightforward to assume that each pathway is linear, so that its response to the sum of two stimuli is equal to the sum of the responses to each stimulus alone. The question is, can the temporal response properties of LEDs be explained by relatively sluggish excitatory inputs that are summed postsynaptically with inhibitory inputs having a higher temporal bandwidth? This notion was tested by recording the responses to sinusoidal flicker stimulation at two temporal frequencies, a low frequency of 0.125 Hz and a high frequency of 4 Hz. Contrary to the prediction of the linear model, the LEDs did not generate any spikes for the two superimposed temporal frequencies (Fig. 12*A*, bottom record). Examination of the synaptic conductances shows how this linear model fails. The linear predictions for the excitatory and inhibitory conductances are compared with the actual responses in Figure 12*C*. For inhibition, the sum of the components was very similar to the dual-component response. In contrast, the excitatory conductance deviated strongly from the linear prediction, because of the lack of the low-frequency component. Therefore, although postsynaptic inhibitory conductances appear to be important for determining the temporal properties of LEDs, additional nonlinearities within

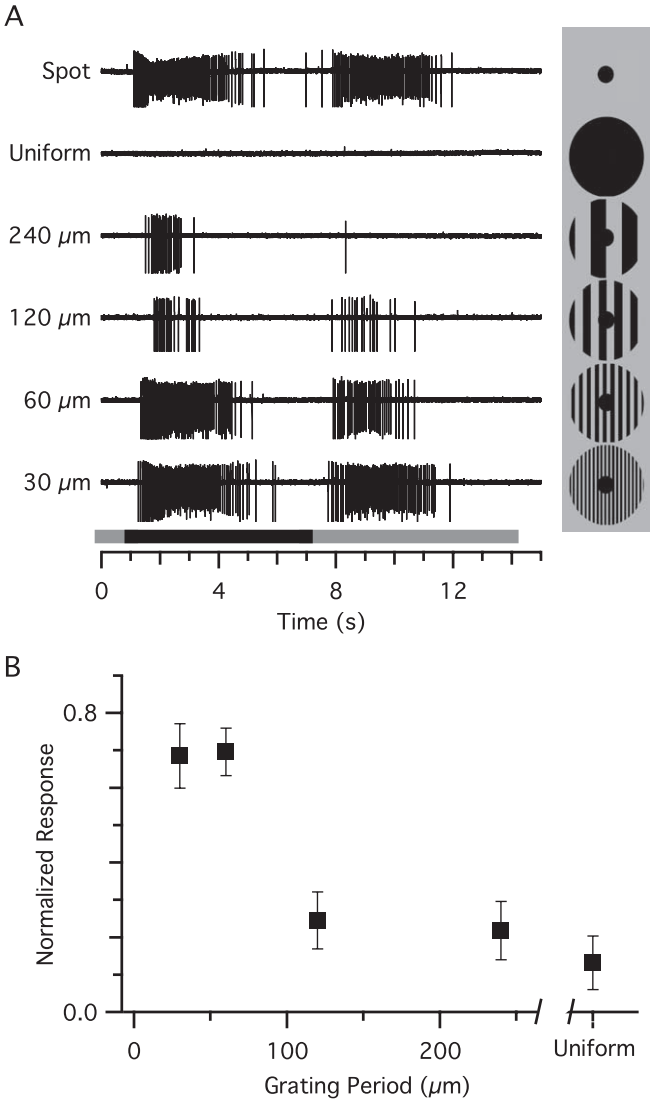

Figure 9. Spatial tuning of the antagonistic surround. ***A***, Spike records obtained for the stimuli shown to the right of each record; the stimulus timing and contrast sign are shown by the bar below the spike records. The spot diameter was 100 μm and the surround diameter was 850 μm; the spatial period of the surround gratings is shown to the left of each record. ***B***, Mean response ($\pm$SEM) of six cells to the stimuli shown in ***A***. Responses are the combined spike counts during the On and Off responses, and are normalized to the response for the center spot alone.

the presynaptic excitatory circuitry may also play a role. An obvious possibility is that high-frequency stimulation produces sustained inhibition of the excitatory bipolar cell terminals that are presynaptic to the LEDs.

Discussion

LED cell density and visual acuity

The proposition that the spatial acuity of the rabbit visual system could be set by the LED array under some conditions requires that the LEDs are present at a sufficient density and have appropriately small receptive fields. Given that several lines of evidence from this study indicate that the LEDs account for only ~15% of all ganglion cells in the rabbit retina, is there independent evidence that no other type of ganglion cell is present at higher density?

Marc and Jones (2002) identified 14 types of ganglion cells in the rabbit retina based on the molecular phenotypes of the so-

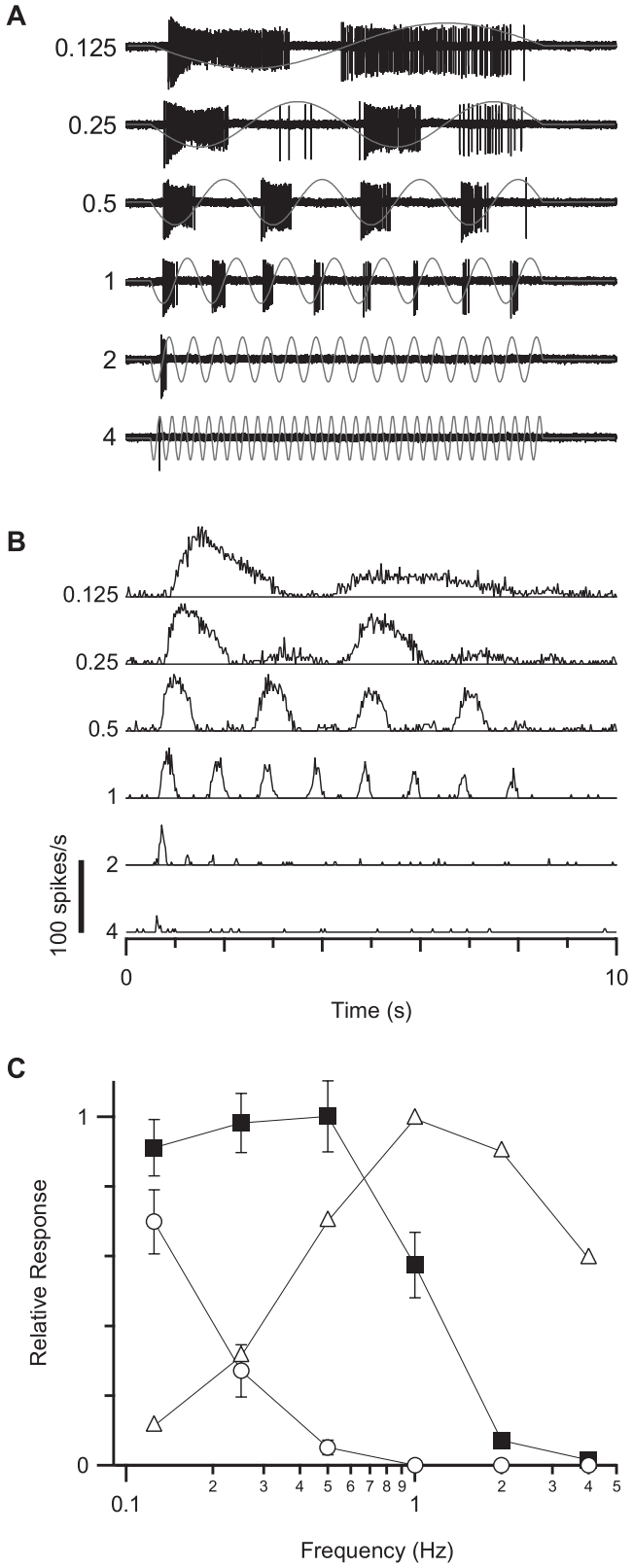

Figure 10. Temporal response properties of LEDs. ***A***, Spike responses elicited by sinusoidal flicker stimuli (gray) at the temporal frequencies (in hertz) indicated to the left of each record; the stimulus was a center spot of 100 μm diameter at $\pm$80% contrast. ***B***, Spike-time histograms accumulated from 10 cells; the ordinate is the spike frequency per trial (10 ms bins). ***C***, Mean normalized response amplitude ($\pm$SEM) versus stimulus frequency for seven LEDs (black squares, Off response; white circles, On response) and one On-center brisk-sustained cell (white triangles). Response amplitude was calculated as the total number of spikes elicited during the On or Off response for an 8 s stimulus.

mata. The most common type (class 6) accounted for 15% of the ganglion cells; their small somata (13 μm diameter) formed a regular mosaic, thus providing confidence that they comprise a single functional type (Wässle and Riemann, 1978). The class 6 cells contained elevated levels of GABA but not glycine, whereas the LEDs might be expected to have elevated levels of both neurotransmitters, given that they show tracer coupling to both GABAergic and glycinergic amacrine cells (Fig. 4*B*,*C*) (Vaney et al., 1998). The class 7 ganglion cells did show such a phenotype, but they accounted for only 5.6% of the ganglion cells and their somata were irregularly distributed. If the class 6 cells do correspond to the LEDs, the neurotransmitter coupling between the glycinergic amacrine cells and the LEDs must have been rather weak in Marc and Jones' tissue, as was the tracer coupling in many of our own preparations.

Is the density of LEDs high enough to account for the visual acuity of the rabbit? Both behavioral studies and cortical evoked-potential measurements have shown that the rabbit has a grating acuity of 3 cycles/° (van Hof, 1967; Kulikowski, 1978; Vaney, 1980a), which corresponds to 1 cycle/56 μm on the retina (Hughes and Vaney, 1981). To resolve such a grating without aliasing, Shannon's sampling theorem requires that the detectors be spaced no more than 28 μm apart. Indeed, the closest LEDs observed in this study were separated by 28 μm and the smallest LEDs had dendritic fields of only 49–53 μm diameter However, based on a larger sample of dye-injected cells, we estimated that the LEDs in the peak visual streak have a somatic spacing of 39 $\pm$ 5 μm, raising doubts about whether the LEDs could provide the substrate for high-acuity vision. But it is clear that other types of ganglion cells with wider dendritic trees, including the On brisk-sustained cells or the Off brisk-sustained cells, would not be present at sufficient density to resolve a grating of 3 cycles/° on their own, unless the dendritic-field overlap was significantly greater than that of the LEDs.

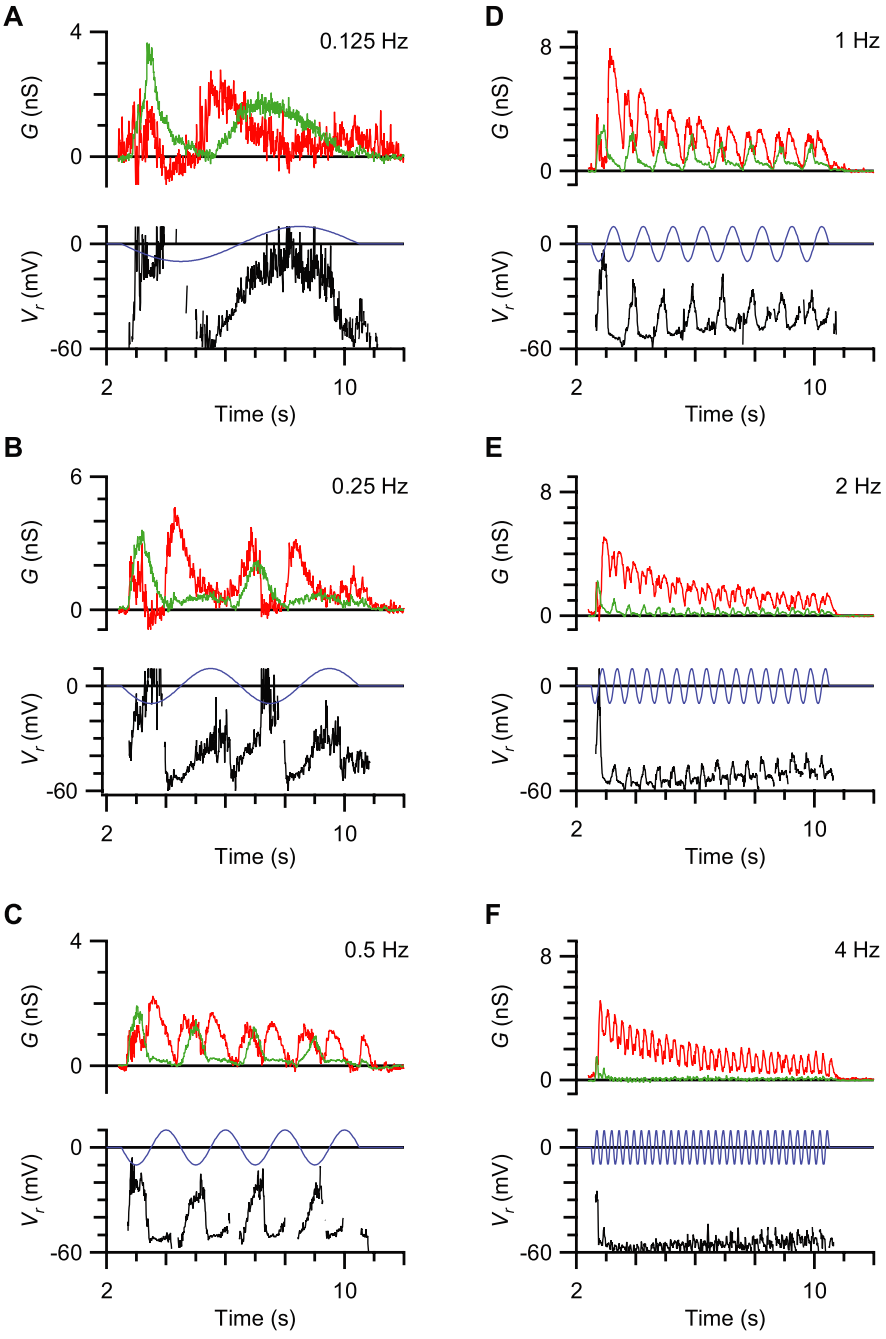

Figure 11. Temporal properties of excitatory and inhibitory synaptic inputs. ***A–F***, Each of the six panels shows the synaptic conductance and reversal potentials for a different stimulus frequency (0.125–4 Hz), calculated as in Figure 8. In each case, the top panel shows the calculated excitatory conductance (green) and inhibitory conductance (red); the bottom panel shows the stimulus timing (blue) and the synaptic reversal potential (black).

The morphology and physiology of the presumptive LEDs in the cat retina appear to be very similar to those of the definitive LEDs in the rabbit retina, with the visual acceptance angle of cat LEDs being only ~50% larger than the rabbit LEDs (Berson et al., 1998). In contrast, the brisk-sustained/X-cells show greater quantitative differences, being noticeably larger than the LEDs in the rabbit retina and much smaller than the LEDs in the cat retina (Roska and Werblin, 2001; Zeck et al., 2005). The cat's need to hunt fast-moving prey at close quarters has favored development of the X-cell system, which operates at high temporal frequencies. The rabbit's need to detect predators during visual fixation, when high temporal frequencies are minimal, may have favored development of the LED system, which operates at low temporal frequencies.

Synaptic mechanisms of spatial processing

The synaptic conductance measurements indicated that there was a clear separation between the neuronal pathways mediating the spatial and temporal properties of the LEDs. The spatial response properties appeared to be mediated mostly by presynaptic mechanisms, evident as a strong suppression of both the excitatory and inhibitory inputs to the LEDs when the surround was stimulated. Differences between the On and Off inputs in the

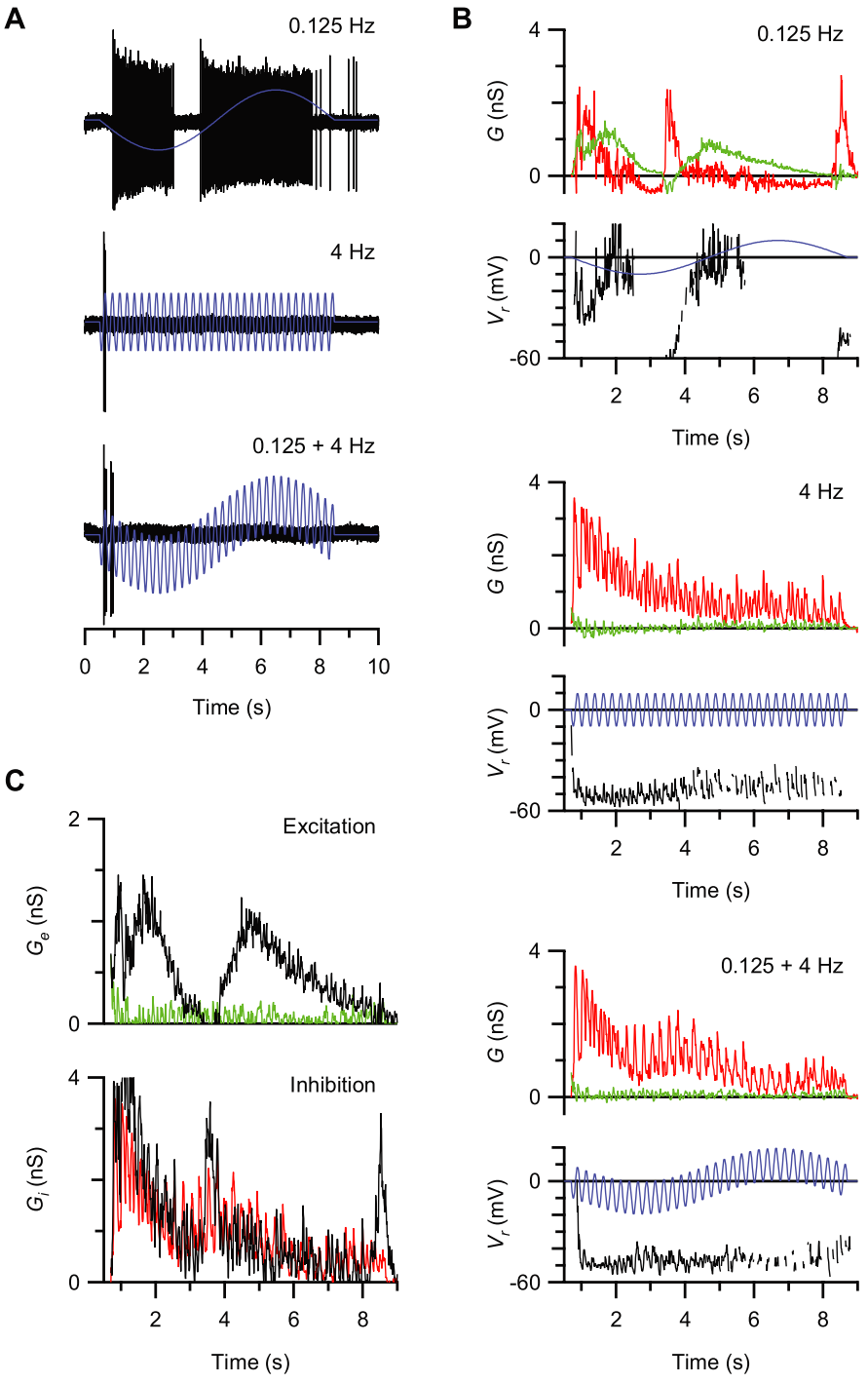

Figure 12. Nonlinearities in temporal response characteristics. The sinusoidal flicker stimulus (blue) was a center spot of 100 μm diameter. ***A***, Spike recordings (black) showing responses to 0.125 Hz (top record), 4 Hz flicker (middle record), and 0.125 + 4 Hz flicker (bottom record); the peak-to-peak stimulus contrast was $\pm$40% for single frequencies and $\pm$80% for the superimposed frequencies. ***B***, The measured reversal potentials (V_r; black) and the calculated excitatory (green) and inhibitory (red) synaptic conductances are shown for each flicker stimulus. ***C***, The black lines show the linear prediction obtained by adding together the conductance components for the 0.125 Hz stimulus and 4 Hz stimulus (***B***, top and middle panels); the green and red lines show the actual conductance components for the combined 0.125 + 4 Hz stimulus (***B***, bottom panel).

degree and the spatial extent of the surround suppression suggest that the surround is mediated by distinct amacrine cells in the On and Off pathways. Such presynaptic suppression is also apparent in the patch-clamp recordings made from rabbit LEDs by Roska and Werblin (2001) (their Fig. 3*C*); moreover, they also found that the On responses were elicited over a narrow range of spot sizes (50–200 μm diameter), whereas the Off responses were elicited by spots up to 500 μm in diameter

Presynaptic surround inhibition might include both horizontal cell inhibition in the outer retina and amacrine cell inhibition in the inner retina. Although the current results do not allow us to distinguish between these possibilities, the effects of gratings in the surround strongly support the idea that much of the surround inhibition is generated in the inner retina by amacrine cells (Fig. 9) (Thibos and Werblin, 1978; Demb et al., 1999; Taylor, 1999; Flores-Herr et al., 2001; Roska and Werblin, 2001). The surround suppression decreased as the spatial frequency of the surround grating was increased, suggesting that these amacrine cells are most responsive at an optimal spatial frequency and become essentially blind to the highest frequencies. These results are consistent with the original finding of Levick (1967) that LEDs are inhibited by edges in their surround.

The essential "local" responsiveness of local edge detectors is therefore established presynaptic to the ganglion cells themselves, presumably at the level of the bipolar cell terminals driving the LEDs. Interestingly, a recent electron microscope study by Famiglietti (2005a) showed that cone bipolar cells provided 40% of the synaptic input to an LED but only 20% to the On–Off direction-selective ganglion cells, whose synaptic input was dominated by amacrine cells. These findings led Famiglietti to propose that the trigger feature of LEDs is formed by presynaptic integration. Our study shows that this is the case in the spatial domain, but the situation in the temporal domain is more complex.

Synaptic mechanisms of temporal processing

The temporal tuning of the On-spike responses of LEDs was strikingly different from that of the Off-spike responses: the On responses were much more sluggish than the Off responses and they ceased at temporal frequencies above ~0.25 Hz (Fig. 10). Conductance measurements indicated that the sluggish responses reflect in part sluggish bipolar cell inputs, with the On bipolar cells being considerably slower than the Off bipolar cells. During flicker stimulation, the On excitation was slower to rise and more sustained than the Off excitation (Fig. 11). Moreover, at the lowest frequency, the On excitation was less than the Off excitation, and with increasing frequency, the On excitation became more strongly attenuated than the Off excitation. It will be interesting to determine whether these differences arise in the outer retina as differences in glutamate receptor prop-

erties in the bipolar cells (Awatramani and Slaughter, 2000; DeVries, 2000), or whether they arise in the inner retina because of GABAergic inhibition (Dong et al., 1994; Nirenberg and Meister, 1997) or differences in the transmitter release properties.

A consequence of the slower On inputs is that, at the lowest temporal frequencies, the LEDs showed frequency doubling, signaling the presence of an edge within the receptive-field center, regardless of contrast but, at higher frequencies between ~0.25 and 1 Hz, the LEDs became Off-center cells exclusively, and thus also signaled the sign of the contrast border. This was also apparent in the responses to pseudorandom checkerboard stimuli, which showed that, for such stimuli, the LEDs are essentially Off-center cells (Fig. 7) (DeVries, 1999; Xu et al., 2005; Zeck et al., 2005; Berry, 2006). The dominance of the Off inputs under some conditions suggests that quantitative models of LED function based primarily on their On responses are unlikely to capture the spatial and temporal complexity of the LEDs (Zeck et al., 2005).

The synaptic conductance measurements indicate that differences in the excitatory inputs are not the only mechanism of temporal tuning. During flicker stimulation, the On inhibition was comparable with, or slightly greater than the Off inhibition at all temporal frequencies. The high temporal bandwidth of the inhibitory inputs was also evident from the synaptic conductances elicited by step changes in intensity. The inhibition was faster to activate than the excitation (Figs. 5, 8), with the result that the synaptic reversal potential was initially held to a negative value before depolarizing, consistent with the sluggish onset of spiking during step responses. Such temporal disparities between the inhibitory and excitatory inputs to rabbit LEDs are also apparent in the patch-clamp recordings made by Roska and colleagues (Roska and Werblin, 2001; Roska et al., 2006). Considering that the inhibitory inputs reach the ganglion cell through an additional synapse, the results suggest either that the bipolar cells driving the excitatory inputs to the LEDs are distinct from those driving the inhibitory amacrine cells, or that some mechanism compensates for the additional synaptic delay.

The findings from the present study suggest that the temporal tuning of LEDs does not result solely from the intrinsic temporal properties of the excitatory inputs, but rather from the postsynaptic integration of excitatory and inhibitory inputs with different temporal properties. Although the postsynaptic integration of inputs appears to be important for temporal tuning, it is clearly not the whole story. We showed that the superposition of a high-frequency flicker on a low-frequency flicker appeared to suppress the response to the low-frequency stimulus, an effect that appeared to be selective for the excitatory inputs. Such inhibition generated by high frequencies has a natural correlate in the suppression of LED spiking by stimuli that were designed to mimic saccadic eye movements (Roska and Werblin, 2003). These rapid global shifts in natural scenes also blocked several other types of ganglion cells that ramified in the middle of the inner plexiform layer, and it will be interesting to find out whether these ganglion cells receive inputs from the same types of bipolar and amacrine cells that drive the LEDs.

References

Amthor FR, Oyster CW (1995) Spatial organization of retinal information about the direction of image motion. Proc Natl Acad Sci USA 92:4002–4005.

Amthor FR, Takahashi ES, Oyster CW (1989) Morphologies of rabbit retinal ganglion cells with complex receptive fields. J Comp Neurol 280:97–121.

Awatramani GB, Slaughter MM (2000) Origin of transient and sustained responses in ganglion cells of the retina. J Neurosci 20:7087–7095.

Berry MJ (2006) Studying the population code of the retina. In: Proceedings MEA meeting 2006 (Stett A, ed), pp 82–85. Stuttgart, Germany: BIOPRO Baden-Württemberg GmbH.

Berson DM, Pu M, Famiglietti EV (1998) The zeta cell: a new ganglion cell type in cat retina. J Comp Neurol 399:269–288.

Borg-Graham LJ (2001) The computation of directional selectivity in the retina occurs presynaptic to the ganglion cell. Nat Neurosci 4:176–183.

Bormann J, Hamill O, Sakmann B (1987) Mechanism of anion permeation through channels gated by glycine and γ-aminobutyric acid in mouse cultured spinal neurones. J Physiol (Lond) 385:243–286.

Buhl EH, Peichl L (1986) Morphology of rabbit retinal ganglion cells projecting to the medial terminal nucleus of the accessory optic system. J Comp Neurol 253:163–174.

Caldwell JH, Daw NW (1978) New properties of rabbit retinal ganglion cells. J Physiol (Lond) 276:257–276.

Caldwell JH, Daw NW, Wyatt HJ (1978) Effects of picrotoxin and strychnine on rabbit retinal ganglion cells: lateral interactions for cells with more complex receptive fields. J Physiol (Lond) 276:277–298.

Cleland BG, Levick WR (1974) Properties of rarely encountered types of ganglion cells in the cat's retina and an overall classification. J Physiol (Lond) 240:457–492.

Dacey DM (1989a) Axon-bearing amacrine cells of the macaque monkey retina. J Comp Neurol 284:275–293.

Dacey DM (1989b) Monoamine-accumulating ganglion cell type of the cat's retina. J Comp Neurol 288:59–80.

Dacey DM (1993) The mosaic of midget ganglion cells in the human retina. J Neurosci 13:5334–5355.

Demb JB, Haarsma L, Freed MA, Sterling P (1999) Functional circuitry of the retinal ganglion cell's nonlinear receptive field. J Neurosci 19:9756–9767.

DeVries SH (1999) Correlated firing in rabbit retinal ganglion cells. J Neurophysiol 81:908–920.

DeVries SH (2000) Bipolar cells use kainate and AMPA receptors to filter visual information into separate channels. Neuron 28:847–856.

DeVries SH, Baylor DA (1997) Mosaic arrangement of ganglion cell receptive fields in rabbit retina. J Neurophysiol 78:2048–2060.

Dong CJ, Picaud SA, Werblin FS (1994) GABA transporters and GABAC-like receptors on catfish cone- but not rod-driven horizontal cells. J Neurosci 14:2648–2658.

Ehinger B, Florén I (1976) Indoleamine-accumulating neurons in the retina of rabbit, cat and goldfish. Cell Tissue Res 175:37–48.

Famiglietti EV (2005a) Synaptic organization of complex ganglion cells in rabbit retina: type and arrangement of inputs to directionally selective and local-edge-detector cells. J Comp Neurol 484:357–391.

Famiglietti EV (2005b) "Small-tufted" ganglion cells and two visual systems for the detection of object motion in rabbit retina. Vis Neurosci 22:509–534.

Flores-Herr N, Protti DA, Wässle H (2001) Synaptic currents generating the inhibitory surround of ganglion cells in the mammalian retina. J Neurosci 21:4852–4863.

Hampson ECGM, Vaney DI, Weiler R (1992) Dopaminergic modulation of gap junction permeability between amacrine cells in mammalian retina. J Neurosci 12:4911–4922.

Hughes A, Vaney DI (1981) Contact lenses change the projection of visual field onto rabbit peripheral retina. Vision Res 21:955–956.

Koch K, McLean J, Segev R, Freed MA, Berry MJ, Balasubramanian V, Sterling P (2006) How much the eye tells the brain. Curr Biol 16:1428–1434.

Kulikowski JJ (1978) Pattern and movement detection in man and rabbit: separation and comparison of occipital potentials. Vision Res 18:183–189.

Levick WR (1967) Receptive fields and trigger features of ganglion cells in the visual streak of the rabbit's retina. J Physiol (Lond) 188:285–307.

MacNeil MA, Heussy JK, Dacheux RF, Raviola E, Masland RH (1999) The shapes and numbers of amacrine cells: matching of photofilled with Golgi-stained cells in the rabbit retina and comparison with other mammalian species. J Comp Neurol 413:305–326.

Marc RE, Jones BW (2002) Molecular phenotyping of retinal ganglion cells. J Neurosci 22:413–427.

Masland RH, Mills JW, Hayden SA (1984) Acetylcholine-synthesizing amacrine cells: identification and selective staining by using radioautography and fluorescent markers. Proc R Soc Lond B Biol Sci 223:79–100.

Menger N, Pow DV, Wässle H (1998) Glycinergic amacrine cells of the rat retina. J Comp Neurol 401:34–46.
Nirenberg S, Meister M (1997) The light response of retinal ganglion cells is truncated by a displaced amacrine circuit. Neuron 18:637–650.
Oesch N, Euler T, Taylor WR (2005) Direction-selective dendritic action potentials in rabbit retina. Neuron 47:739–750.
Oyster CW, Takahashi ES, Hurst DC (1981) Density, soma size, and regional distribution of rabbit retinal ganglion cells. J Neurosci 1:1331–1346.
Pourcho RG, Goebel DJ (1985) A combined Golgi and autoradiographic study of (^{3}H)glycine-accumulating amacrine cells in the cat retina. J Comp Neurol 233:473–480.
Pow DV, Wright LL, Vaney DI (1995) The immunocytochemical detection of amino-acid neurotransmitters in paraformaldehyde-fixed tissues. J Neurosci Methods 56:115–123.
Provis JM (1979) The distribution and size of ganglion cells in the regina of the pigmented rabbit: a quantitative analysis. J Comp Neurol 185:121–137.
Rockhill RL, Daly FJ, MacNeil MA, Brown SP, Masland RH (2002) The diversity of ganglion cells in a mammalian retina. J Neurosci 22:3831–3843.
Rodieck RW, Stone J (1965) Analysis of receptive fields of cat retinal ganglion cells. J Neurophysiol 28:832–849.
Rodieck RW, Watanabe M (1993) Survey of the morphology of macaque retinal ganglion cells that project to the pretectum, superior colliculus, and parvicellular laminae of the lateral geniculate nucleus. J Comp Neurol 338:289–303.
Roska B, Werblin F (2001) Vertical interactions across ten parallel, stacked representations in the mammalian retina. Nature 410:583–587.
Roska B, Werblin F (2003) Rapid global shifts in natural scenes block spiking in specific ganglion cell types. Nat Neurosci 6:600–608.
Roska B, Molnar A, Werblin FS (2006) Parallel processing in retinal ganglion cells: how integration of space-time patterns of excitation and inhibition form the spiking output. J Neurophysiol 95:3810–3822.
Sagar SM (1986) NADPH diaphorase histochemistry in the rabbit retina. Brain Res 373:153–158.
Sandell JH, Masland RH (1988) Photoconversion of some fluorescent markers to a diaminobenzidine product. J Histochem Cytochem 36:555–559.
Taylor WR (1999) TTX attenuates surround inhibition in rabbit retinal ganglion cells. Vis Neurosci 16:285–290.
Taylor WR, Vaney DI (2002) Diverse synaptic mechanisms generate direction selectivity in the rabbit retina. J Neurosci 22:7712–7720.
Thibos LN, Werblin FS (1978) The properties of surround antagonism elicited by spinning windmill patterns in the mudpuppy retina. J Physiol (Lond) 278:101–116.
van Hof MW (1967) Visual acuity in the rabbit. Vision Res 7:749–751.
Vaney DI (1980a) The grating acuity of the wild European rabbit. Vision Res 20:87–89.
Vaney DI (1980b) A quantitative comparison between the ganglion cell populations and axonal outflows of the visual streak and periphery of the rabbit retina. J Comp Neurol 189:215–233.
Vaney DI (1984) "Coronate" amacrine cells in the rabbit retina have the "starburst" dendritic morphology. Proc R Soc Lond B Biol Sci 220:501–508.
Vaney DI (1986) Morphological identification of serotonin-accumulating neurons in the living retina. Science 233:444–446.
Vaney DI (1990) The mosaic of amacrine cells in the mammalian retina. Prog Retinal Res 9:49–100.
Vaney DI (1991) Many diverse types of retinal neurons show tracer coupling when injected with biocytin or Neurobiotin. Neurosci Lett 125:187–190.
Vaney DI (1994) Territorial organization of direction-selective ganglion cells in rabbit retina. J Neurosci 14:6301–6316.
Vaney DI (2003) Retinal amacrine cells. In: The visual neurosciences (Chalupa LM, Werner JS, eds), pp 395–409. Cambridge, MA: MIT.
Vaney DI (2004) Type 1 nitrergic (ND1) cells of the rabbit retina: comparison with other axon-bearing amacrine cells. J Comp Neurol 474:149–171.
Vaney DI, Young HM (1988) GABA-like immunoreactivity in NADPH-diaphorase amacrine cells of the rabbit retina. Brain Res 474:380–385.
Vaney DI, Levick WR, Thibos LN (1981) Rabbit retinal ganglion cells: receptive field classification and axonal conduction properties. Exp Brain Res 44:27–33.
Vaney DI, Nelson JC, Pow DV (1998) Neurotransmitter coupling through gap junctions in the retina. J Neurosci 18:10594–10602.
van Wyk M (2006) Local edge detectors in the rabbit retina. PhD thesis, The University of Queensland.
Velte TJ, Masland RH (1999) Action potentials in the dendrites of retinal ganglion cells. J Neurophysiol 81:1412–1417.
Wässle H (2004) Parallel processing in the mammalian retina. Nat Rev Neurosci 5:1–11.
Wässle H, Riemann HJ (1978) The mosaic of nerve cells in the mammalian retina. Proc R Soc Lond B Biol Sci 200:441–461.
Wässle H, Boycott BB, Illing R-B (1981) Morphology and mosaic of on- and off-beta cells in the cat retina and some functional considerations. Proc R Soc Lond B Biol Sci 212:177–195.
Xu Y, Dhingra NK, Smith RG, Sterling P (2005) Sluggish and brisk ganglion cells detect contrast with similar sensitivity. J Neurophysiol 93:2388–2395.
Zeck GM, Xiao Q, Masland RH (2005) The spatial filtering properties of local edge detectors and brisk-sustained retinal ganglion cells. Eur J Neurosci 22:2016–2026.